

Single-pulse drilling study on Au, Al and Ti alloy by using a picosecond laser

J. Cheng · W. Perrie · M. Sharp · S.P. Edwardson · N.G. Semaltianos · G. Dearden · K.G. Watkins

Received: 12 June 2008 / Accepted: 8 December 2008 / Published online: 23 December 2008
© Springer-Verlag 2008

Abstract Picosecond laser single pulse ablation of Au, Al and Ti alloy (Ti6Al4V) was experimentally investigated with a laser pulse width of 10 ps at a wavelength of 1064 nm for potential industrial micromachining applications. The diameters, depths and morphologies of the drilled craters were studied. Two novel phenomena were found: as hole diameters decreased with fluence, a change of slope of the trend line indicated a change in ablation mechanism for Al and Ti alloy, metallic materials with short electron-phonon coupling times (< 10 ps), while Au showed no such transition: an isolated island structure was also observed on Au due to significant melt expulsion. A one-dimensional two-temperature model has been used to discriminate different ablation phenomena. It is shown that metallic materials with different electron-phonon coupling constant have different ablation characteristics in the ps regime. This study could be very helpful for metallic material micromachining with high repetition rate ps lasers pulses which indicates that high throughput may be achieved as well as good machining quality.

PACS 52.75.Di · 52.38.Mf · 79.20.Ds

J. Cheng (✉) · W. Perrie · S.P. Edwardson · N.G. Semaltianos · G. Dearden · K.G. Watkins
Department of Engineering, University of Liverpool, Liverpool, UK, L69 3GH
e-mail: Jian.Cheng@liv.ac.uk
Fax: +44-151-650-2304

J. Cheng
Institute of Thermal Science & Technology, Shandong University, Shandong, China, 250061

M. Sharp
Lairdside Laser Engineering Centre, Wirral, Merseyside, UK, CH41 9HP

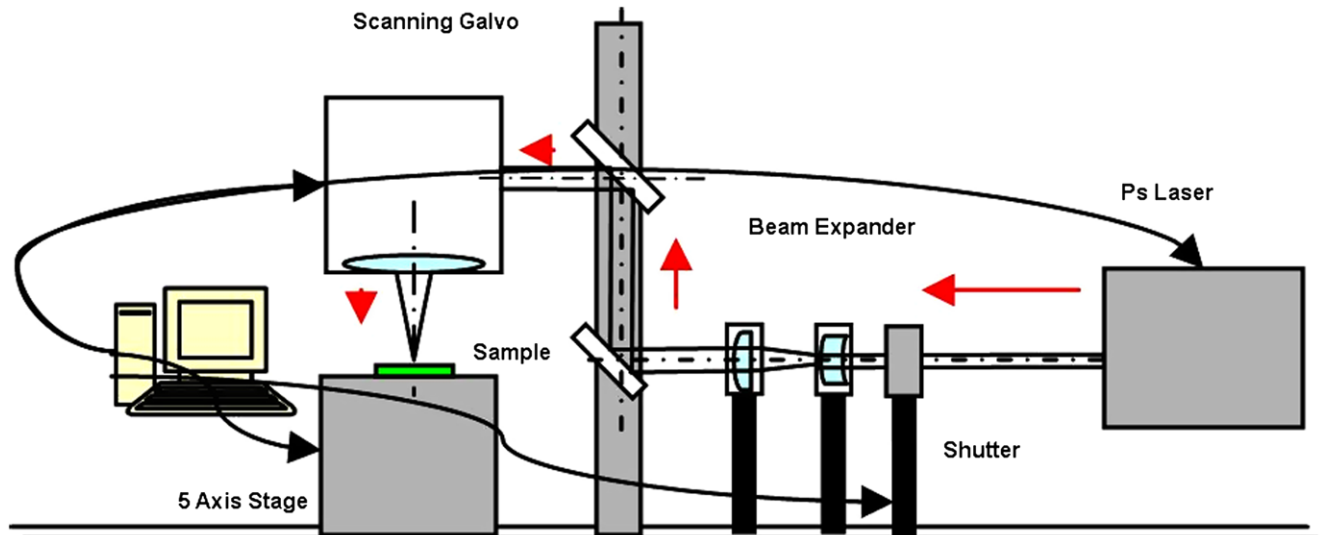
1 Introduction

Micromachining using femtosecond laser pulses has been widely investigated in recent years because of its potential for high precision and almost melt-free processing of materials. While the observed processing quality meets industrial demands, processing speed is, however, still far from adequate for industrial use [1]. Ultrafast pulse lasers with significantly higher average power and repetition rate than currently available will be required to overcome this limitation [2]. Compared to complex and expensive femtosecond laser systems requiring Chirped Pulse Amplification, picosecond laser systems with compact scale, high average power output and repetition rate may show significant advantages over femtosecond lasers. From a laser-materials interaction point of view, Dausinger argued that the mere reduction of pulse duration does not guarantee good machining quality and suggested that a pulse duration of 5 to 10 ps appears to be optimal for micromachining, especially for metals [3]. A number of research groups has shown that picosecond laser micromachining can produce high machining quality combined with efficiency [4–7].

According to the one-dimensional two-temperature model, metals with different electron-phonon coupling constants should have their own corresponding coupling time ranges. Hence, for micro-structuring a metal with coupling time in the ps regime, which is the timescale required for the lattice to reach thermal equilibrium, the temporal pulse width, whether fs or ps, should play only a minor role. In this article, experimental results of single pulse drilling of three metallic materials are presented: Au, Al and Ti alloy (Ti6Al4V), with widely varying electron-phonon coupling constants (see Table 1) by using a single 10 ps laser pulse at 1064 nm wavelength. This is very useful to reveal aspects of ps laser metallic material micro-structuring mechanism

Table 1 Physical properties of the three selected metals

	Metals		
	Au ^a	Al ^a	Ti6Al4V ^b
Heat Capacity, C_l ($\times 10^6 \text{ J m}^{-3} \text{ K}^{-1}$)	2.5	2.43	2.33
Electron-Phonon Coupling Constant, g ($\times 10^{16} \text{ W m}^{-3} \text{ K}^{-1}$)	2.1	56.9	40
Melting Temperature, T_m (K)	1337	933	1941
Vaporization Temperature, T_v (K)	3081	2740	3560
Heat Conductivity, K ($\text{W m}^{-1} \text{ K}^{-1}$)	318	238	6.7
Latent Heat of Melting, L_m (J g^{-1})	64.9	388	390
Latent Heat of Evaporation, L_v (J g^{-1})	1738	10800	8854

^aData are from literature [8, 9]^bPart of data are referred from element Ti**Fig. 1** Schematic illustration of the experimental set-up for single-pulse picosecond laser drilling. The laser beam goes along the path of the red arrows as shown and finally focuses at the sample surface

without the complication of multipulse incubation effects. Finally, the response of the materials after the laser pulse drilling is investigated, by studying the morphologies of the machined features which may be relevant to industrial application.

2 Experimental setup

The laser used in this work was a custom made seeded Nd:VAN regenerative amplifier laser system (High Q, Photonics Solutions) capable of running at up to 50 kHz repetition rate with output wavelengths at 1064 nm, 532 nm and 355 nm. Maximum pulse energy at 1064 nm was measured to be $>250 \mu\text{J}$ and temporal pulse width $\tau_p = 10 \text{ ps}$ (FWHM), confirmed with an autocorrelator, while measured pulse-to-pulse stability was excellent, $<0.5\%$. A pulse picker followed the regenerative amplifier output hence allowing single pulse to be selected by applying an appropriate TTL signal to the controller. In addition, an internal attenuator, software controlled, was used to vary the output

pulse energy. Figure 1 shows the schematic of the experimental set-up. The output beam traversed a beam expander [$M = 3$] and was then directed to a scanning galvanometer with $f = 100 \text{ mm}$ f -theta lens (Nutfield). Focused spot size was observed to be $\sim 22 \mu\text{m}$, almost diffraction limited. Metallic material samples of Au, Al and Ti alloy were mounted on a 5-axis Aerotech precision motion control system running under NView MMI, which has a resolution of $0.5 \mu\text{m}$. For these three metallic materials, the pulse energy was increased from $0.2 \mu\text{J}$ to $100 \mu\text{J}$ and a series of holes drilled by single pulse.

The micro-machining dimensions were observed with a Nikon optical microscope with CCD camera and residual surface features and ablation depths determined using a WYKO NT1100 optical surface profiling system.

3 Results

The expected $1/e^2$ focused spot size ($2\omega_0$) at the substrate surface can be calculated from the following equation [10]:

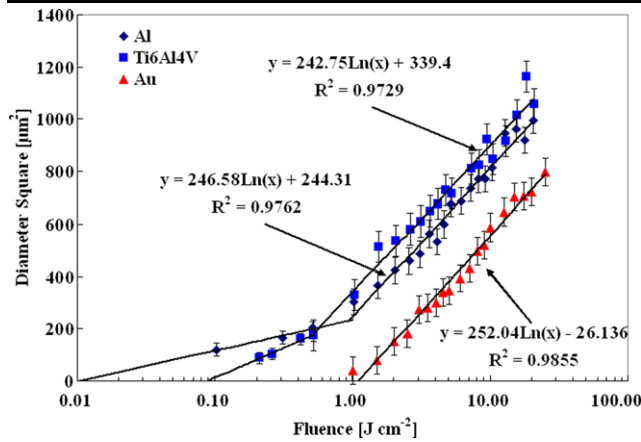


Fig. 2 Plot of Diameter Squared of single-pulse drilled holes against logarithmic fluence. The data fit $D^2 = 2\omega_0^2 \ln(\phi_0/\phi_{th})$ reasonably well when fluence is above 1 J cm^{-2} . The slopes indicate the spot diameter is about $22 \pm 0.2 \text{ }\mu\text{m}$. The *solid line* represents the least-squares fit according to (2)

$$2\omega_0 = \frac{4}{\pi} \lambda \frac{f}{d} M^2, \tag{1}$$

where ω_0 is the radius of beam waist, λ ($1.064 \text{ }\mu\text{m}$) is the wavelength, f (100 mm) is the focal length of the f-theta lens, d (6.3 mm) is the diameter of expanded laser beam and M^2 (1.1) is the beam quality factor. Using these values, the focused waist diameter $2\omega_0 = 23.8 \text{ }\mu\text{m}$.

Since the beam is near Gaussian, the ablated hole diameter D , as a function of fluence ϕ , should follow the equation [11]:

$$D^2 = 2\omega_0^2 \ln(\phi/\phi_{th}), \tag{2}$$

where ϕ_{th} is the ablation threshold. Figure 2 shows a plot of the measured diameter squared versus fluence on a logarithmic scale for the three metals indicating satisfactory agreement with (2) under median laser fluence between 1 J cm^{-2} and 30 J cm^{-2} . The slopes $2\omega_0^2$ are similar and infer a focused spot size of $22 \pm 0.2 \text{ }\mu\text{m}$, close to the theoretical value of $23.8 \text{ }\mu\text{m}$ indicating excellent beam quality. By extrapolation of D^2 to zero, the values for the ablation threshold fluence, $\phi_{th\text{-Ablation}}$ can be inferred to be 0.24 J cm^{-2} , 0.37 J cm^{-2} and 1.1 J cm^{-2} for Ti6Al4V, Al and Au, respectively. These values should be higher than those of multishot experiments due to the lack of incubation effect.

From Fig. 2, it can be seen that in the case of Al and Ti alloy, there is clear change of slope below fluence $< 1 \text{ J cm}^{-2}$, indicating a change in the ablation mechanism, while for Au no such regime exists. This may well be due to the relative contribution of evaporation versus melting as peak intensity is reduced and supported by the observed small burrs around the irradiated areas (see Figs. 5a and 6a). By extrapolation of D^2 to zero again, the values for the melting threshold fluence, $\phi_{th\text{-Melting}}$ can be inferred to be 0.09 J cm^{-2} and

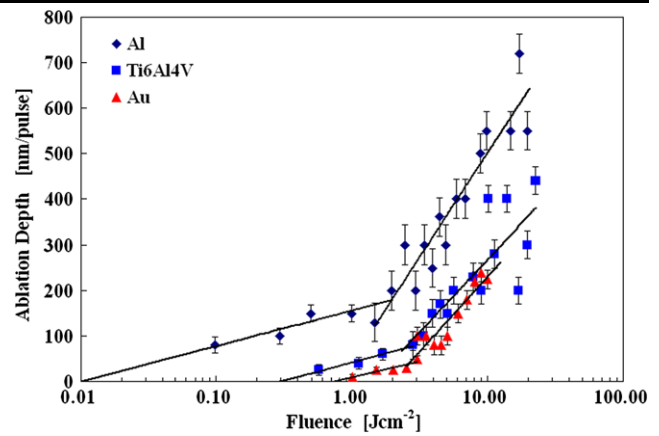


Fig. 3 Variation of ablation rate with laser fluence for 10 ps pulse duration laser ablation. The *plot* shows that a two-stage ablation mechanism applies. The *solid line* represents the least-squares fit according to (3) and (4)

0.01 J cm^{-2} for Ti alloy and Al, respectively. Allowing for the significant difference in melting points of Ti alloy and Al (1649 K and 933 K, respectively, Table 1), the lower indicated melting threshold of Al from Fig. 2 can be understood.

By measuring the holes depth with the WYKO NT1100 optical surface profiling system, the ablation rate could be deduced. For single-pulse drilled holes, a spread in measured depth was observed; hence hole depths were estimated by averaging over five drilled holes at each fluence, indicated by the error bars in Fig. 3. Hole depth and hence the ablation rate are shown as functions of laser fluence.

These results also indicate two stages of ablation, similar to that observed with femtosecond pulses [12, 13]: for low laser influence, the ablation rate per pulse can be described by the expression:

$$L = \alpha^{-1} \ln(\phi/\phi_{th}^\alpha), \tag{3}$$

where L is the ablation rate per pulse, α^{-1} is the optical penetration depth, and ϕ_{th}^α is the threshold fluence. For high laser influence, the ablation rate per pulse can be described by the expression:

$$L = \ell \ln(\phi/\phi_{th}^\ell), \tag{4}$$

where L is the ablation rate per pulse, ℓ is the electron heat diffusion depth, and ϕ_{th}^ℓ is the threshold fluence.

The slopes for fluence $< 3 \text{ J cm}^{-2}$ in Ti alloy and Al indicate optical penetration depths of 39 and 42 nm, respectively, and increasing to 128 and 258 nm for higher fluence. The optical penetration depths for Al of 42 nm and 258 nm coincide with the value Le Harzic has reported of 40 nm and 260 nm, respectively [14]. In Au, the low fluence regime indicates an optical penetration depth of 30 nm and increasing to 190 nm when fluence was above 5 J cm^{-2} due to electron diffusion.

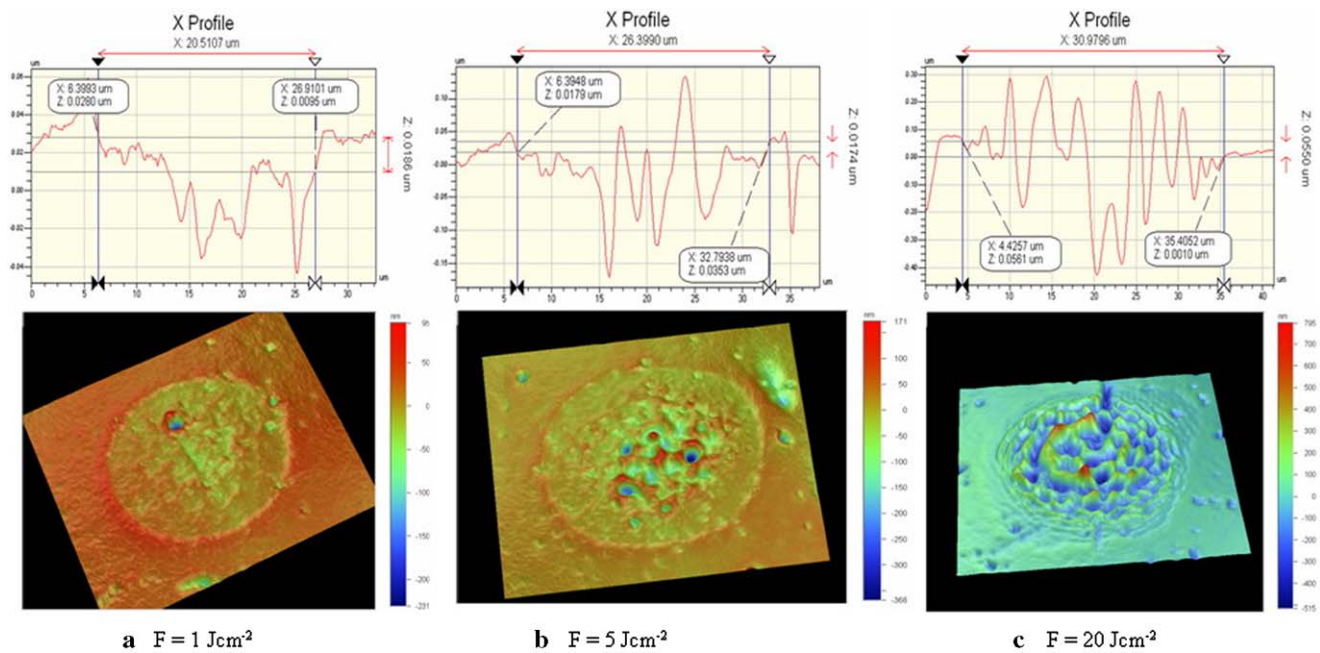


Fig. 4 Cross section profiles (upper) and 3-D images (lower) of single-pulse drilling of Ti alloy sample under varied laser fluence: (a) $F = 1 \text{ Jcm}^{-2}$, ~ 4 times ablation threshold; (b) $F = 5 \text{ Jcm}^{-2}$, ~ 20 times ablation threshold; (c) $F = 20 \text{ Jcm}^{-2}$, ~ 80 times ablation threshold

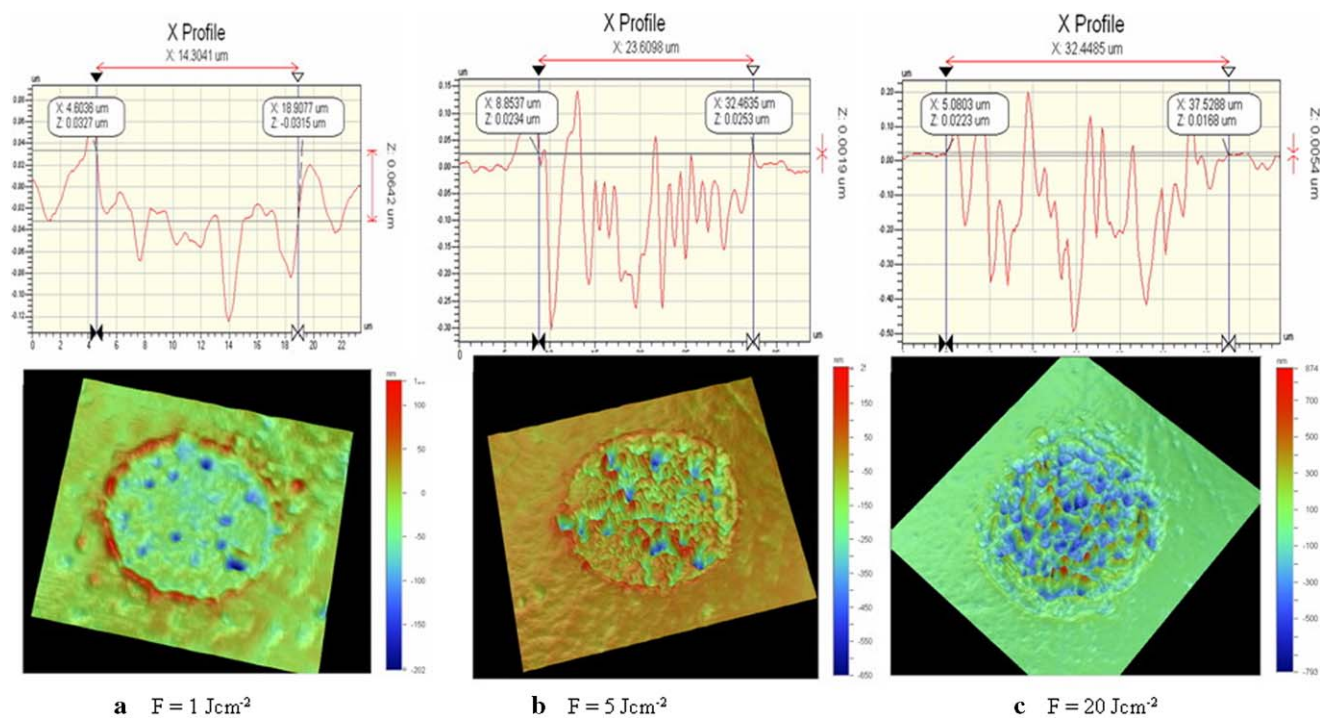


Fig. 5 Cross section profiles (upper) and 3-D images (lower) of single-pulse drilling of Al sample under varied laser fluence: (a) $F = 1 \text{ Jcm}^{-2}$, ~ 3 times ablation threshold; (b) $F = 5 \text{ Jcm}^{-2}$, ~ 14 times ablation threshold; (c) $F = 20 \text{ Jcm}^{-2}$, ~ 54 times ablation threshold

Figures 4, 5 and 6 show cross section profiles of single shot ablation of these three metallic materials with an increasing laser fluence of 1, 5 and 20 Jcm^{-2} and their respective 3D surface features. Under a fluence of 1 Jcm^{-2} ,

the hole depth is greatest for Al at about 100 nm at the centre of the hole. The depths for Ti alloy and for Au are approximately 40 nm and 25 nm, respectively. There is a much deeper 200 nm circular slot along the edge area for

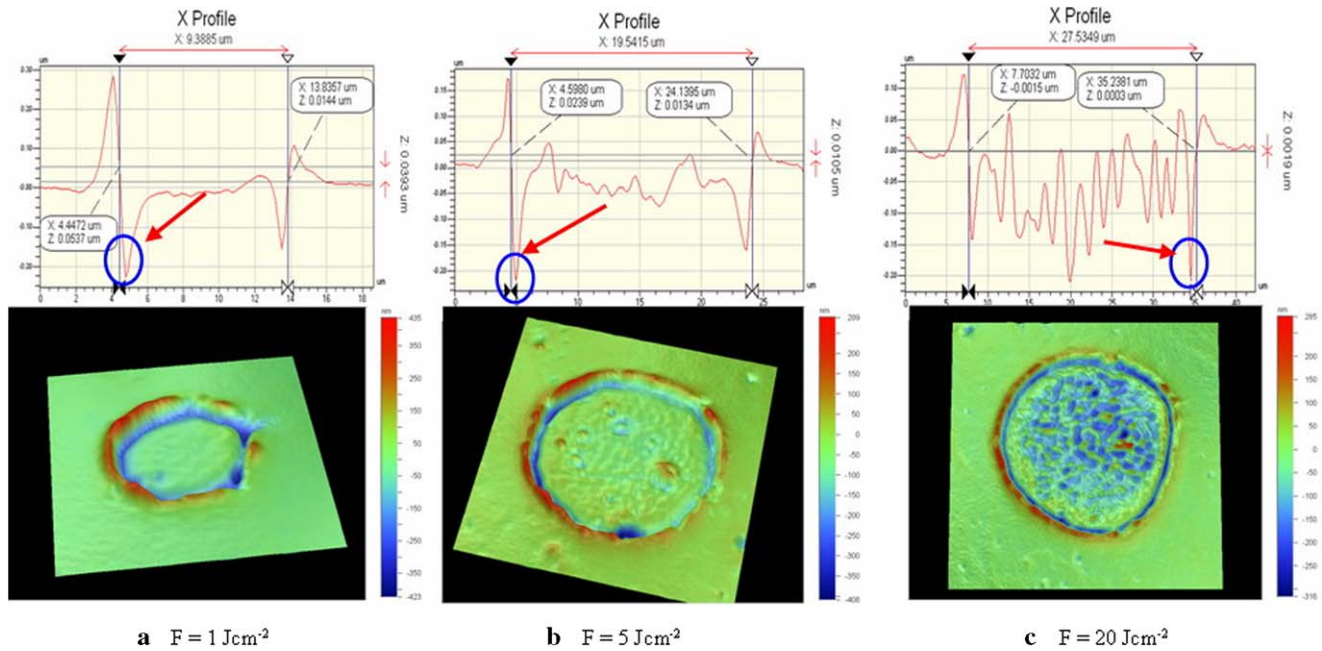


Fig. 6 Cross section profiles (*upper*) and 3-D images (*lower*) of single-pulse drilling of Au sample under varied laser fluence: (a) $F = 1 \text{ J cm}^{-2}$, \sim ablation threshold; (b) $F = 5 \text{ J cm}^{-2}$, \sim 5 times ablation threshold; (c) $F = 20 \text{ J cm}^{-2}$, \sim 20 times ablation threshold.

The depths of *red arrows* pointed at (*blue colour circled areas*) showed almost the same average value of 200 nm no matter what the laser fluence were

Au. When the fluence is increased above 5 J cm^{-2} , Ti alloy and Al come into the second stage of ablation: the hole depth of Ti alloy is 150 nm and 250 nm for Al. Meanwhile, Au is still at the end of the first ablation stage with hole depth of 50 nm in the central area and 200 nm for the circular slot in the outside edge area. When fluence rises to 20 J cm^{-2} , all three metallic materials are in the second ablation stage. Indications of shock wave effects on the Ti alloy sample were observed with hole depth of 400 nm. Hole depth on Al was 600 nm due to evaporation followed by significant phase explosion. In the case of Au, the observed residual micro-structure is quite different from Al and Ti alloy: there is evidence of evaporation and melt expulsion, shown by the smooth central area surrounded by a circular burr.

4 Discussion

Single-pulse 10 ps ablation experiments on three metallic materials selected here for the wide variation in electron–phonon coupling constant, g , demonstrate quite different ablation characteristics. The one-dimensional two-temperature model is considered to explain the observed phenomena. This model describes temperature dynamics [15–17] as follows:

$$C_e \frac{\partial T_e}{\partial t} = -\frac{\partial}{\partial z} \left(k \frac{\partial T_e}{\partial t} \right) - g(T_e - T_l) + S(z, t), \quad (5)$$

$$C_l \frac{\partial T_l}{\partial t} = g(T_e - T_l), \quad (6)$$

where C_e and C_l are the electronic and phonon heat capacities, respectively. The first equation describes (i) electron diffusion (k is the electron thermal conductivity), (ii) electron–phonon coupling (coupling constant g), and (iii) heating of the electrons by the laser pulse (the source term $S(z, t)$ is the absorbed laser energy density per unit time). The diffusive term is absent in the second equation, because heat diffusion occurs much more rapidly through the electron gas than through lattice phonons.

From (5), one must compare results at the same absorbed energy density. For 1064 nm wavelength, reflectivity is strongly dependent on electrical conductivity. Metallic materials with high electrical conductivity have higher values of infrared reflectivity [18]. For example, Au has about 3 times higher reflectivity than Al at room temperature. However, reflectivity decreases, as a rule, with rising temperature [19]. Wang et al. measured the time-resolved electron-temperature of Au suggesting the electron system could get to a high temperature of 0.3 eV in less than 1 ps [20]. Therefore, it can be assumed for the first ps, these metallic materials have different reflectivity and after that, because of the high electron temperature, the real absorbed laser energy is approximately the same on each metallic material.

In this experiment, electron–phonon coupling time for Au is about 119 ps, 4.3 ps for Al and 5.8 ps for Ti alloy according to Chichkov’s method of $\tau_{ep} = C_l/g$ [21] and data

from Table 1, which means that the lattice will essentially reach thermal equilibrium during the temporal pulse length for Al and Ti alloy but certainly not for Au until much later at time $t > 100$ ps. The different electron–phonon coupling times can also be used to explain the slope changes observed in Fig. 2 for Al and Ti alloy, while none is observed for Au under low fluence of 1 J cm^{-2} . Both Ti alloy and Al have electron–phonon coupling time less than 10 ps, which means stronger energy transfer ability from electron subsystem to lattice and then large lattice temperature gradients. Figure 7 shows that for a Gaussian beam, there should be a melting threshold, $\phi_{\text{th-Melting}}$, an ablation threshold, $\phi_{\text{th-Ablation}}$, and their respective laser-irradiated diameters D_{Melting} and D_{Ablation} . When the laser fluence rises to above approximately $>1 \text{ J cm}^{-2}$, the high fluence regime, then D_{Melting} and D_{Ablation} are similar, and the slopes with higher gradient (Fig. 2) are determined by the ablation diameter from which the focused spot diameter is deduced. As fluence and hence peak intensity is reduced, the relative contribution of melting becomes more important, determining the surface morphology. The observed slopes in the case of Al and Ti alloy when extrapolated to zero may well indicate the melt threshold. In the case of Au, which has such a long electron–phonon coupling time leading to melting, the single threshold corresponds to this melting threshold.

Referring to Fig. 3 on the measured ablation rates with fluence, the low threshold regimes below a fluence of about $1\text{--}3 \text{ J cm}^{-2}$, demonstrate laser pulse coupling determined by the optical penetration depth in the metallic materials and emphasises the effect of electron–phonon coupling without

the complication of significant surface plasma. Then, the melting threshold can be roughly estimated as

$$\phi_{\text{th-Melting}} = \frac{(C_l T_m + L_m)h}{1 - R}, \quad (7)$$

where R is the reflectivity, and h is the melting layer thickness. Taking the optical penetration depths of 42 and 39 nm for Al and Ti alloy, respectively, as h and $R = 0.7$ (an estimated value for mild laser intensity) into (7), the melting thresholds of 0.03 J cm^{-2} and 0.07 J cm^{-2} for Al and Ti alloy are estimated respectively, in reasonable agreement with experimental values.

From Figs. 4, 5 and 6, it can be seen that under 1 J cm^{-2} , Al and Ti alloy have approximately the same diameter since their electron–phonon coupling times are similar, while Au has much smaller diameter because of its long electron–phonon coupling time and hence larger ablation threshold. Surface profiles of the holes for Al and Ti alloy look much rougher and deeper than Au, which suggests much stronger electron–phonon coupling and hence more ablation in these two metallic materials.

From Fig. 6, it can be seen that, for Au, the deepest area was not in the centre of the hole according to the laser intensity profile but along the circular edge, generating an isolated island independent of laser fluence. The depth of these circular slots varied from 200–400 nm. For this phenomenon, according to Sparks et al. [23], heat diffusion length can be described as follows:

$$\ell = 2\sqrt{\kappa\tau_{\text{ep}}}, \quad (8)$$

where ℓ is the heat diffusion length, κ is the heat diffusivity of the material, and τ_{ep} is the electron–phonon coupling time. For Au, $\kappa = 1.28 \text{ cm}^2 \text{ s}^{-1}$, $\tau_{\text{ep}} = 119$ ps, hence the heat diffusion depth is 240 nm, coincident with the slot depth shown on Fig. 6. Therefore it is clear that it is the electron–phonon coupling time, not the pulse width, which determines the ablation in Au. Figure 8, for comparison, shows the single-pulse ablation results on Au with a 180 fs pulse width at a wavelength of 775 nm (Clark-MXR 2010). Clearly, circular slots still occur along the irradiated area boundary with depths measured again to be $\sim 200\text{--}400$ nm, as with 10 ps pulses. The observed surface structure on Au is clearly determined by heat diffusion since ℓ (heat diffusion length) \gg optical penetration depth and almost independent of temporal pulse width.

As for the burr edges, the long electron–phonon coupling time combined with the high thermal conductivity in Au allows the lattice to transfer heat more evenly in the irradiated area. Just above ablation threshold, the liquid phase dominates, and melt expulsion generates the circular burr edge as molten material gets drawn from the central region. Eventually, the material cools and solidifies to create the island structure.

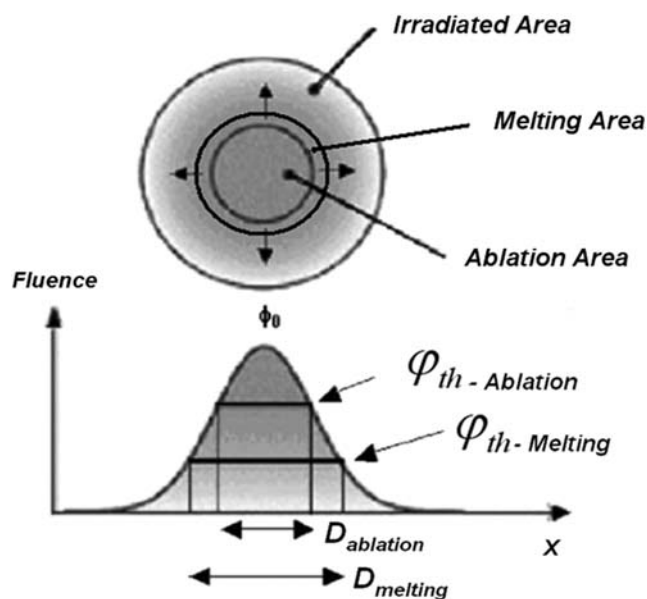


Fig. 7 Schematic illustration of melting regime and ablation regime for metallic materials with short electron–phonon coupling time. Note: part of this figure is referred from [22]

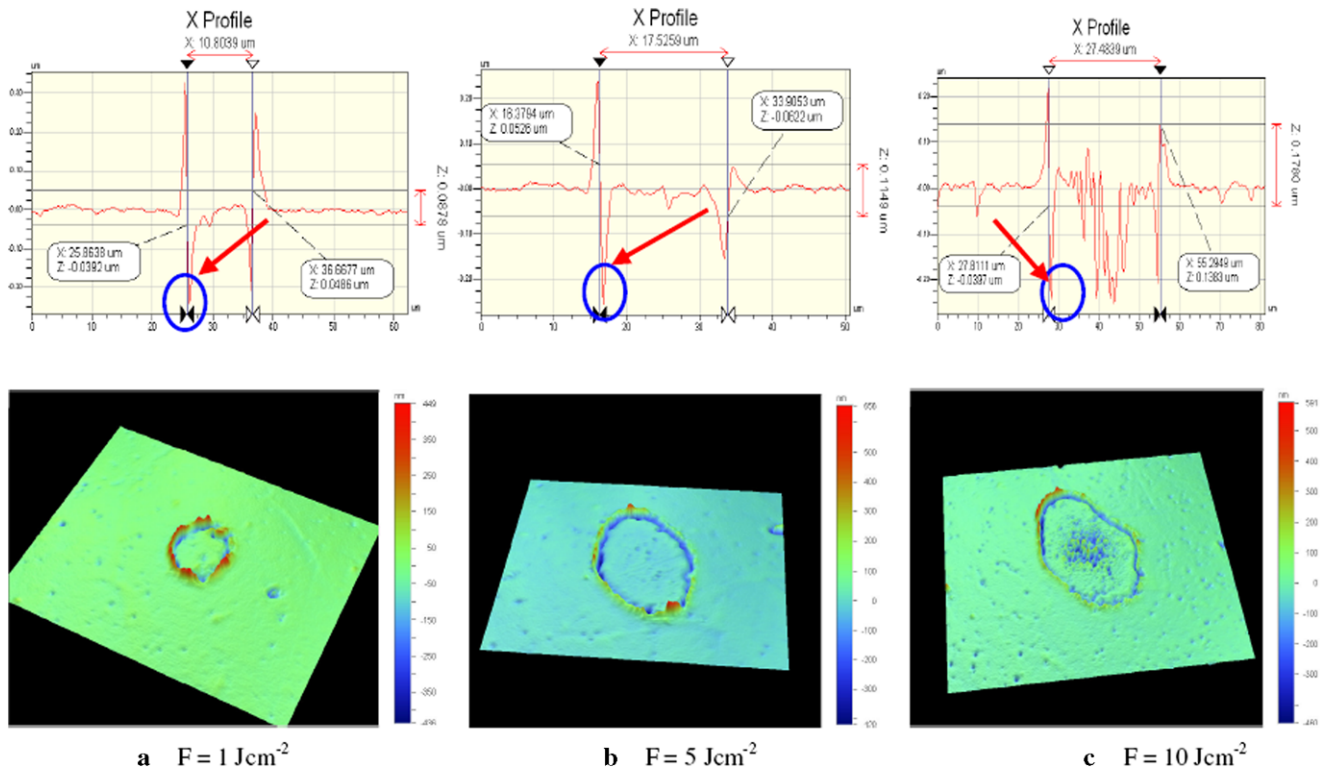


Fig. 8 Cross section profiles (*upper*) and 3-D images (*lower*) of single-pulse drilling of Au sample by using a 180 fs laser at a wavelength of 775 nm under varied laser fluence: (a) $F = 1 \text{ J cm}^{-2}$, (b) $F =$

5 J cm^{-2} , (c) $F = 10 \text{ J cm}^{-2}$. The depth at the positions shown by the *red arrows* suggested that even for a 180 fs pulse length, at least 100 ps is required for the laser energy to be coupled into the lattice

5 Conclusions

Picosecond laser single-pulse drilling of Au, Al and Ti alloy was experimentally studied with laser pulse duration of 10 ps for potential micromachining applications. This work demonstrates that two ablation regimes occur on Al and Ti alloy during single pulse 10 ps ablation. Melting thresholds of 0.09 J cm^{-2} and 0.01 J cm^{-2} and ablation threshold of 0.24 J cm^{-2} and 0.37 J cm^{-2} for Ti alloy and Al, respectively, were found. Al and Ti alloy, with strong electron-phonon coupling, ablate easily and above 1 J cm^{-2} show evidence of strong phase explosion, while Au shows significant melting, melt expulsion and consequent burr formation, expected because of its long electron-phonon coupling time. Comparative ablation on Au with fs pulses demonstrates near identical surface geometry with burrs. Further experiments of multipulse drilling and micro structuring are underway to evaluate 10 ps laser ablation quality and throughput for industrial applications.

Acknowledgements The authors gratefully acknowledge the support of the North West Development Agency (NWDA) in the UK. The author J. Cheng would like to thank UK/China Postgraduate Research Scholarships for Excellence and the China Scholarships Council for their financial support.

References

1. J. König, S. Nolte, A. Tünnermann, *Opt. Express* **13**, 10597 (2005)
2. F. Dausinger, F. Lichter, H. Lubatschowski, *Femtosecond Technology for Technical and Medical Applications* (Springer, Heidelberg, 2004)
3. F. Dausinger, *Proc. SPIE* **5777**, 840 (2005)
4. G. Račiukaitis, M. Brikas, *Proc. SPIE* **5662**, 717 (2004)
5. A. Ostendorf, G. Kamlage, U. Klug, F. Korte, B.N. Chichkov, *Proc. SPIE* **5713**, 1 (2005)
6. D. Karnakis, G. Rutterford, M. Knowles, T. Dobrev, P. Petkov, S. Dimov, *Proc. SPIE* **6106**, 610604 (2006)
7. J. Lleinbauer, R. Knappe, R. Wallenstein, *Appl. Phys. B* **80**, 315 (2005)
8. R. Le Harzic, D. Breitling, M. Weikert, S. Sommer, C. Föhl, S. Valette, C. Donnet, E. Audouard, F. Dausinger, *Appl. Surf. Sci.* **249**, 322 (2005)
9. S.D. Broson, A. Kazeroonian, J.S. Moodera, D.W. Face, T.K. Cheng, E.P. Ippen, M.S. Dresselhaus, G. Dresselhaus, *Phys. Rev. Lett.* **64**, 2172 (1990)
10. W.M. Steen, K. Watkins, *Laser Material Processing*, 3rd edn. (Springer, London, 2003)
11. J.M. Liu, *Opt. Lett.* **7**, 196 (1982)
12. S. Nolte, C. Momma, H. Jacobs, A. Tünnermann, B.N. Chichkov, B. Wellegehausen, H. Welling, *J. Opt. Soc. Am. B* **14**, 2716 (1997)
13. S. Preuss, A. Demchuk, M. Stuke, *Appl. Phys. A* **61**, 33 (1995)
14. R. Le Harzic, D. Breitling, M. Weikept, S. Sommer, C. Föhl, F. Sausinger, S. Valette, C. Donnet, E. Audouard, *Appl. Phys. A* **80**, 1589 (2005)

15. S.I. Anisimov, B. Kapeliovich, T.L. Perel'man, *Sov. Phys. JETP* **39**, 375 (1974)
16. S.-S. Wellershoff, J. Hohlfeld, J. Güdde, E. Matthias, *Appl. Phys. A* **69**(Suppl.), 99 (1999)
17. M. Bonn, D.N. Denzler, S. Funk, M. Wolf, S.-S. Wellershoff, J. Hohlfeld, *Phys. Rev. B* **61**, 1101 (2000)
18. J.F. Ready, *LIA Handbook of Laser Material Processing* (Magnolia Publishing, 2001)
19. M.V. Allmen, A. Blatter, *Laser-Beam Interactions with Materials* (Springer, Heidelberg, 1994)
20. X.Y. Wang, D.M. Riffe, Y.-S. Lee, M.C. Downer, *Phys. Rev. B* **50**, 8016 (1994)
21. B.N. Chichkov, C. Momma, S. Nolte, F. von Alvensleben, A. Tünnermann, *Appl. Phys. A* **63**, 109 (1996)
22. P.T. Mannon, J. Magee, E. Coyne, G.M. O'Connor, T.J. Glynn, *Appl. Surf. Sci.* **233**, 275 (2004)
23. M. Sparks, E. Loh, *J. Opt. Soc. Am.* **69**, 847 (1976)